Electrocatalytic Site Activity Enhancement via Orbital Overlap in A_2MnRuO_7 ($A = Dy^{3+}$, Ho^{3+}, Er^{3+}) Pyrochlore Nanostructures

V. Celorrio[a,b,*], D. Tiwari,[a,c,*] L. Calvillo,[d] A. Leach,[e, f] H. Huang,[e] G. Granozzi,[d] J.A. Alonso,[g] A. Aguadero,[h] R.M. Pinacca,[i] A.E. Russell,[c] and D.J. Fermin[a,*]

[a]School of Chemistry, University of Bristol. Cantocks Close. BS8 1TS Bristol, UK

[b]Current Address: Diamond Light Source Ltd. Diamond House. Harwell Campus. Didcot, OX11 0DE, UK.

[c]Current Address: Department of Mathematics, Physics & Electrical Engineering, Northumbria University, Newcastle upon Tyne NE1 8ST, UK

[d]Dipartimento di Scienze Chimiche, Università di Padova, Via F. Marzolo 1, 35131 Padova, Italy

[e]School of Chemistry, University of Southampton. Highfield, Southampton, SO17 1BJ, UK.

[f]Current address: Electrochemical Innovation Lab, Department of Chemical Engineering, University College London, London WC1E 7JE, UK. The Faraday Institution, Harwell Science and Innovation Campus, Didcot OX11 0RA, UK.

[g]Instituto de Ciencia de Materiales de Madrid, C.S.I.C. 28049 Cantoblanco, Madrid, Spain.

[h]Department of Materials, Imperial College. London SW7 2AZ, UK.

[i] INTEQUI, Facultad de Química, Bioquímica y Farmacia, Universidad Nacional de San Luis, San Luis 5700, Argentina

Corresponding Authors:

Veronica Celorrio: veronica.celorrio@diamond.ac.uk

Devendra Tiwari: devendra.tiwari@northumbria.ac.uk

David J. Fermin: david.fermin@bristol.ac.uk

KEYWORDS: pyrochlore oxides, oxygen electrocatalysis, orbital overlap, DFT+U, X-ray absorption/emission, Dy_2RuMnO_7, Ho_2RuMnO_7, Er_2RuMnO_7

ABSTRACT

Oxygen electrocatalysis at transition metal oxides is one of the key challenges underpinning electrochemical energy conversion systems, involving a delicate interplay of bulk electronic structure and surface coordination of the active sites. In this work, we investigate for the first time the structure-activity relationship of A_2RuMnO_7 (A = Dy^{3+}, Ho^{3+}, Er^{3+}) nanoparticles, demonstrating how orbital mixing of Ru, Mn, and O promotes high density of states (DOS) at the appropriate energy range for oxygen electrocatalysis. The bulk and surface structure of these multicomponent pyrochlores are investigated by high-resolution transmission electron microscopy, X-ray diffraction, X-ray absorption (XAS), X-ray emission (XES) and X-ray photoemission (XPS) spectroscopies. The materials exhibit high phase purity (cubic fcc with a space group $Fd\bar{3}m$), in which variations in M-O bonds length are less than 1% upon replacing the *A*-site lanthanide. XES and XPS show that the mean oxidation state at the Mn-site as well as the nanoparticle surface composition were slightly affected by the lanthanide. The pyrochlore nanoparticles are significantly more active than the binary RuO_2 and MnO_2 towards the 4-electron oxygen reduction reaction (ORR) in alkaline solutions. Interestingly, normalization of kinetic parameters by the number density of electroactive sites concludes that Dy_2RuMnO_7 shows twice higher activity than benchmark materials such as $LaMnO_3$. Analysis of the electrochemical profiles supported by DFT calculations reveals that the origin of the enhanced catalytic activity is linked to the mixing of Ru and Mn *d*-orbitals and O *p*-orbitals at the conduction band which strongly overlap with the formal redox energy of O_2 in solution. The activity enhancement strongly manifests in the case of Dy_2RuMnO_7 where Ru/Mn ratio is closer to 1 in comparison with the Ho^{3+} and Er^{3+} analogs. These electronic effects are discussed in the context of the Gerischer formalism for electron transfer at the semiconductor/electrolyte junctions.

TOC GRAPHICS

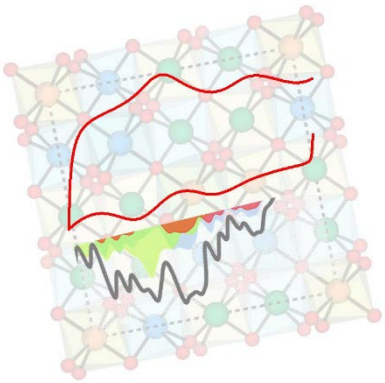

INTRODUCTION

Oxygen electrocatalysis underpins key technologies for the decarbonization of energy production and storage, including fuel cells, water and CO_2 electrolyzers, metal-air batteries and artificial photosynthetic systems.[1-4] Beyond Pt-based electrocatalysts, oxygen electrocatalysis has been widely investigated at transition metal oxides, ranging from binary systems such as IrO_2 and RuO_2 to more compositionally complex structures including perovskites,[5] spinels[6] and pyrochlores.[7] Although a wealth of information has been gathered in this area, establishing structural guiding principles that enable predicting electrocatalytic activity across this vast family of compounds, with such diverse electronic structures, remains a formidable challenge.[8]

A variety of conceptually simple descriptors have been proposed to rationalize activity trends across compounds such as perovskites (ABO_3), including B-site orbital occupancy,[9] oxygen vacancies,[10] B-O covalency,[11] hydroxylation affinity,[12] and oxide enthalpy of formation.[13] These parameters are essentially defined in terms of the bulk structure of the oxide and can often be quantified by X-ray based techniques as well as first-principle electronic structure calculations. In principle, these approaches can establish strategies for guiding de novo design of electrocatalysts as well as high-throughput combinatorial methods.[14] However, numerous experimental observations have shown that these are only parts of a complex picture, in which surface structure and composition as well as orbital occupancy under electrochemical control also play hugely important roles.[15-20] Indeed, electrode potential can introduce substantial changes in surface oxide properties including metal coordination, composition and conductivity. In previous studies, we have linked changes in the oxidation state at the B-site at potentials close to the formal oxygen potential as a key descriptor towards the oxygen reduction reaction to OH^- under alkaline conditions.[21-22] Based on the Gerischer electron transfer formalism,[23-24] this correlation implies

that strongly electron correlated materials require a sizeable density of states overlapping in the energy scale with empty density of states of solvated oxygen molecules. This concept provides a simple rationalization of the high electrocatalytic activity towards the ORR observed in several Mn-based compounds in comparison with other transition metal oxides.[25]

In this work, we shall illustrate the principle of enhancing active electrocatalytic sites by increasing local density around the oxygen formal potential employing pyrochlore nanoparticles with the general formula $A_2B_2O_7$, in which the *A*-site is primarily occupied by Dy^{3+}, Er^{3+} or Ho^{3+}, while the B-site contains Ru and Mn. We employ X-ray diffraction (XRD), X-ray absorption (XAS) as well as X-ray emission spectroscopy (XES) to develop a detailed picture of the structure and oxidation state of metal cations in these complex oxides, which are yet to be investigated in the context of electrocatalysis at the solid/electrolyte interface. X-ray photoelectron spectroscopy (XPS) and electrochemical studies reveal a complex elemental distribution at the oxide surface, which is critically important to rationalize the electrocatalytic activity towards the ORR. We also correlate the electrochemical signatures of these small band gap semiconductors with their electronic structure calculated by DFT+U in order to establish the position of the key orbitals contributing to oxygen electrocatalysis with respect to the reversible hydrogen electrode (RHE).

RESULTS

Structure and surface composition of A_2RuMnO_7 nanoparticles. Pyrochlore nanoparticles were synthesized by thermolysis of citrate-based precursors annealed at 900˚C based on the method described by Martinez-Coronado et al. (see Methods).[26] **Figure 1a** contrasts the powder XRD patterns of the various A_2RuMnO_7 oxides (A = Dy^{3+}, Ho^{3+}, Er^{3+}), which are assigned

to a cubic fcc with a space group $Fd\bar{3}m$, according to ICSD Coll. Codes 169610 and 186272. No secondary phases are observed in the range investigated. The nanocrystalline dimensions of theses oxides are exemplified by high-angle annular dark-field scanning transmission electron microscopy (HAADF-STEM) image of Er_2RuMnO_7 shown in **figure 1b**. Analysis of the TEM images show a narrow size distribution around 60 nm for all pyrochlores (**figure S1**, supporting information), which corresponds to specific surface areas of approximately 14 $m^2\ g^{-1}$ (**table S1**). Nitrogen adsorption-desorption isotherms measured at 77 K provided values of the specific surface area of 4.5 $m^2\ g^{-1}$, calculated using the Brunauer-Emmett-Teller (BET) equation. Both N_2 adsorption and TEM analysis clearly demonstrate that all three pyrochlore nanoparticles are non-porous. Analysis of STEM-EDS mapping for Er-L (**figure 1c**), Ru-L (**figure 1d**), Mn-K (**figure 1e**) and O-K (**figure 1f**) shells show a homogeneous elemental distribution at the individual particle level, which is consistent with the high phase purity revealed by XRD. High-resolution TEM images of Er_2RuMnO_7 particles (**figure S2a-b**) further demonstrate the crystalline nature of the nanoparticles, from which lattice fringes can be clearly observed associated with adjacent {111} planes (**figure S2c**) and interatomic distances in the {222} plane (**figure S2d**). Dy_2RuMnO_7 and Ho_2RuMnO_7 nanoparticles also exhibit a high degree of crystallinity, as shown in selected HRTEM images in **figure S3**.

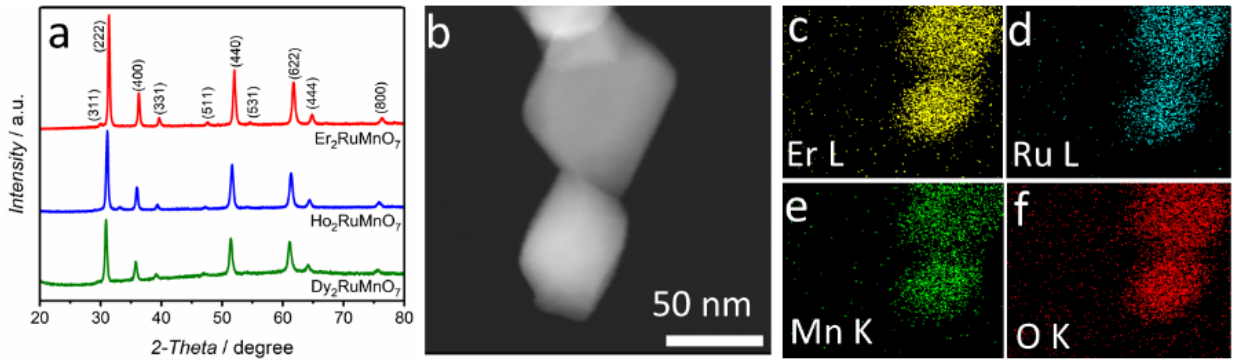

Figure 1. Structure and composition of A_2RuMnO_7 (R = Er, Ho, Dy) pyrochlores nanoparticles. (a) XRD patterns assigned to $Fd\bar{3}m$ showing no secondary phases; (b) HAADF-STEM image of the Er_2RuMnO_7 nanoparticles; EDS elemental maps of (c) Er - L, (d) Ru - L , (e) Mn - K and (f) O - K.

Normalized Ru K-edge and Mn K-edge X-ray absorption spectra of the A_2RuMnO_7 oxide nanoparticles are displayed in **figure 2a** and **c**, respectively. We shall first focus our attention on the XANES region of the spectra, which contains information on the mean oxidation state of the B-sites. In the case of the Ru K-edge, a calibration curve was obtained between the edge position (i.e. the maximum of the first derivative of the spectrum) of suitable reference materials and their corresponding oxidation states as displayed in **figure 2b**. The edge obtained for all three pyrochlores provided values very close to +4, with Dy_2RuMnO_7 and Ho_2RuMnO_7 yielding 4.1 ± 0.7, while Er_2RuMnO_7 resulted in 3.9 ± 0.7. The analysis of the Mn K-edge is significantly more complex due to the wide pre-edge feature (see **figure S4**) and the influence of Mn coordination on the main absorption edge. Although we have analyzed the pre-edge features of Mn perovskites in previous studies,[20-21] in this work, we employed X-ray emission spectroscopy (XES) to probe the effective Mn oxidation state. **Figure 2d** compares the Mn Kβ XES of the different A_2RuMnO_7 nanoparticles (a stacked version of this plot can be found on **Figure S5**), along with the MnO,

Mn_2O_3 and MnO_2 reference systems. The pyrochlore spectra exhibit a main $K\beta_{1,3}$ peak at ~7492 eV and a low-intensity satellite $K\beta'$ line at ~6476 eV. The $K\beta_{1,3}$ peak lies close to that of Mn_2O_3 towards the high energy side, suggesting an effective oxidation state of Mn below the expected +4 value. Based on the method developed by Bordage et al. (see **figure S6**),[27] we can estimate mean Mn oxidation states of +3.5 ± 0.1 (Dy_2RuMnO_7), +3.8 ± 0.6 (Ho_2RuMnO_7) and +3.3 ± 0.1 (Er_2RuMnO_7). The lower effective Mn oxidation state can be linked to partial Mn occupancy in the *A*-site. Indeed, a neutron diffraction study on members of the A_2RuMnO_7 series[26] showed a partial occupancy of the *A*-sites by divalent Mn, since the larger ionic size of this Mn^{2+} ion (0.96 Å) is more adequate to occupy an eightfold oxygen-coordinated position. Neutron diffraction not only unveiled the mixed occupancy of A sites by A^{3+} and Mn^{2+} ions, given their contrasting scattering lengths, but also the lower occupancy of O sites with respect to the full stoichiometry.[26] Therefore, the presence of these oxygen vacancies is linked to the formation of reduced Mn states capable of occupying the *A*-site.

Quantitative analysis of the EXAFS region was performed simultaneously at both edges as displayed in **figure S7**, using the $Fd\bar{3}m$ space group, and keeping fixed coordination numbers, but excluding Mn migration to the *A*-site. The amplitude reduction factor (S_0^2), bond lengths, Debye-Waller factors (σ^2) and the energy shift parameter (ΔE_0) were all refined, with the results shown in **Figure S7** and **Table S2**. High-quality fits were achieved with less than 1% variation in the Mn-O, Mn-Mn_2, Mn-A and Mn-Ru bond lengths for all three pyrochlores. The small variation in bond lengths is consistent with the quantitative refinement of powder neutron diffraction, in which the increase in the *A*-site ionic radii from Er^{3+} to Dy^{3+} manifests itself by an approximate 1% increase in the Mn-O distances and (Ru,Mn)-O-(Ru,Mn) bond angle.[26]

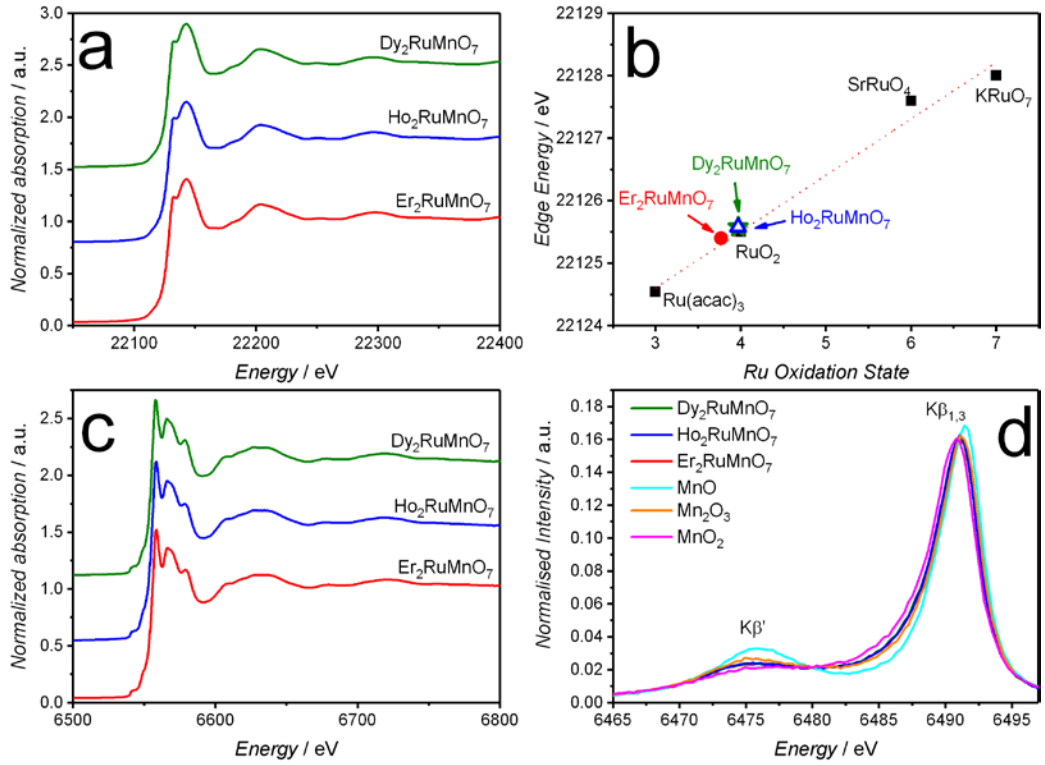

Figure 2. X-Ray Absorption (XAS) and Emission Spectroscopy (XES) of Dy_2RuMnO_7, Ho_2RuMnO_7 and Er_2RuMnO_7 particles. (a) Normalized Ru K-edge XAS and (b) XANES edge position of standards Ru(III)(acetylacetonate)$_3$, RuO_2, $SrRuO_4 \cdot H_2O$, and $KRuO_4$ compounds showing linear correlation with the Ru oxidation state, confirming an effective Ru oxidation state of +4 for all pyrochlores. (c) Normalized Mn K-edge Mn Kβ and (d) XES spectra for all three nanostructures (a stacked version of this plot can be found on Figure S5). Quantitative analysis of the XES data reveals a small fluctuation in the effective Mn oxidation states of +3.5 ± 0.1 (Dy_2RuMnO_7), +3.8 ± 0.6 (Ho_2RuMnO_7) and +3.3 ± 0.1 (Er_2RuMnO_7).

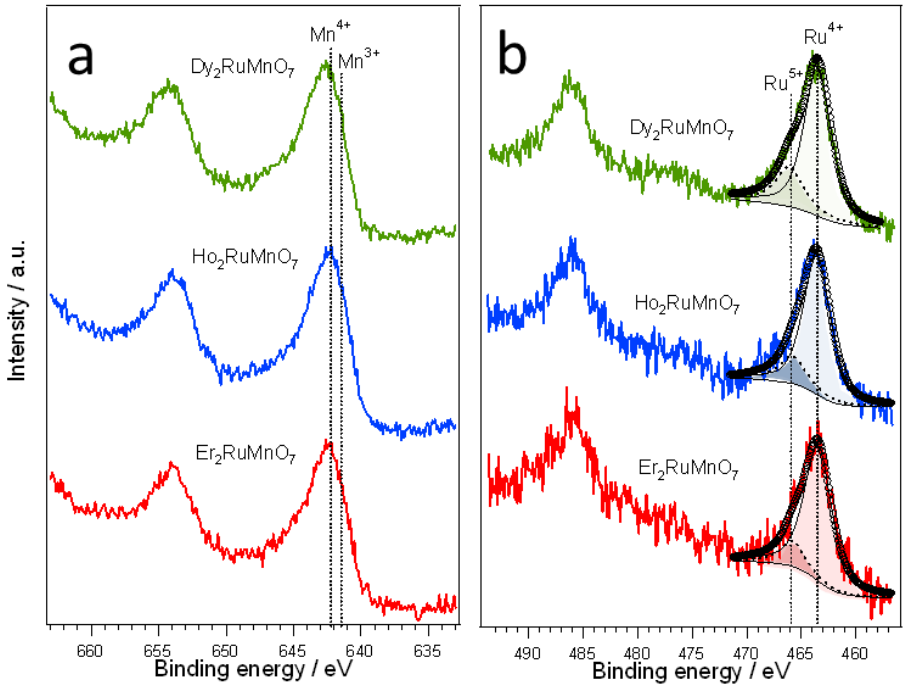

Figure 3. XPS analysis of the B-site cations: (a) Mn 2*p* featuring a broad Mn $2p_{5/2}$ photoemission lines due to the contributions of Mn(III) and Mn(IV) sites; (b) Ru 3*p* revealing contributions from Ru(IV) as well as Ru(V) sites in the Ru $3p_{3/2}$ photoemission region

XPS spectra, recorded using a non-monochromatized Mg Kα source, of the Ru 3*p* and Mn 2*p* regions for the various pyrochlores are contrasted in **figure 3**. Data obtained in the Er 4*d*, Dy 4*d*, Ho 4*d*, Ru 3*d* and O 1*s* spectral regions are displayed in **figure S8**, confirming oxidation state +3 for all lanthanide cations, while the Ru 3*d* lines are rather complex to rationalize due to their strong overlap with the C 1*s* lines. Ru $3p_{3/2}$ peak (**figure 3b**) suggests that Ru is mainly present as Ru^{4+} (binding energy, BE, 463.5 eV) as expected, but also a small amount of Ru^{5+} (BE 465.8 eV) is found at the surface.[28] **Table S3** shows that the ratio of Ru^{4+} to Ru^{5+} varies from 75% in Dy_2RuMnO_7 to 85% in Er_2RuMnO_7. The Ru^{5+} states are most probably confined to the surface of pyrochlore nanostructures, therefore their contributions to the XANES spectra (**figure 2**) would

be negligible. On the other hand, Mn 2*p* lines (**Figure 3a**) show very similar features in all pyrochlores, indicating similar Mn speciation. In view of the overlap in BE of Mn^{4+} (642.2 eV), Mn^{3+} (BE 641.9 eV) and Mn^{2+} (BE 641.7 eV) species in the region corresponding to the Mn $2p_{5/2}$ peak, quantification of the effective Mn surface oxidation state is highly challenging. The presence of Mn sites with oxidation states below +4 is consistent with the bulk picture elucidated from XES. It should also be mentioned that the multiple surface oxidation states of Mn and Ru sites are highly dynamic under electrochemical conditions and this behavior is strongly linked to the electrocatalytic activity. The surface composition of the A_2RuMnO_7 samples was obtained from the A 4*d*, Ru 3*p* and Mn 2*p* peak regions and the corresponding sensitivity factors. The A:Ru:Mn surface atomic ratios are summarized in **Table S4**, showing a significant excess of the *A*-site in the case of Er_2RuMnO_7 ($Er_{2.48}Ru_{0.6}Mn_{0.92}$), while Ho_2RuMnO_7 shows a Mn-rich surface ($Ho_{2.08}Ru_{0.8}Mn_{1.12}$). Dy_2RuMnO_7 shows the closest to the bulk stoichiometry ratio ($Dy_{2.28}Ru_{0.92}Mn_{0.8}$) according to our analysis. As we describe below, whilst the surface compositional variation across this group of pyrochlores may appear small in absolute terms, it does play a key role in determining electrocatalytic activity.

Electrocatalytic activity. Cyclic voltammograms (CV) recorded for the three pyrochlores supported on mesoporous carbon in an Ar-saturated 0.1 M KOH solutions at 0.10 V s^{-1} are shown in **Figure 4a**. As described in previous studies, the pseudo-capacitive responses reveal changes in the oxidation state of redox-active sites at the oxide surface.[17, 19-22] A previous study assigned these electrochemical responses to OH^- lattice intercalation;[29] a process difficult to rationalize in terms of the lattice structure of these oxides as well as direct correlation observed between the charge of the pseudocapacitive responses and the Mn surface ratio.[17, 21] From the solid-state point of view, these redox responses allow mapping the density of states in strongly correlated electron systems

such as these transition metal oxides. All the pyrochlores show two broad peaks between 0.2 and 1.4 V, although the peak potentials and peak current ratios are slightly different. The voltametric responses are stable upon consecutive cycling up to potentials close to 1.7 V vs RHE, suggesting that the surface composition remains unaffected over a wide potential range. However, it should also be acknowledged that surface reconstructions can take place at oxide surfaces which cannot be unambiguously assigned to voltametric features, as recently shown by Gurmelli et al.[30] At constant loading, Ho_2RuMnO_7 displays the largest current while the peaks in Dy_2RuMnO_7 are rather broad spreading up to approximately 1.2 V. The two pseudo-capacitive peaks are qualitatively similar to the highly active $LaMnO_3$ although Ru sites are also expected to contribute in this potential range.[31-32]

As summarized in **Table S5**, integration of the pseudo-capacitive responses provides information on the number density of active redox surface sites (Γ_{sites}) normalized by the oxide loading and specific surface area.[18, 21] **Figure S9** graphically illustrates the approach used for baseline correction in order to calculate the charges associated with the anodic and cathodic features. The baseline position was systematically varied in each voltammogram to compute the impact on the calculation of the areas of the cathodic and anodic peaks, generating a range of values which are reflected in the standard deviation reported in **Table S5**. A key observation arising from this analysis is the increasing value of Γ_{sites} with decreasing surface A:B composition ratio extracted from XPS analysis (**table S4**). Indeed, *A*-site surface segregation follows a trend Er > Dy > Ho, which is the opposite of the current density trend in **figure 4a**. **Table S5** also includes the Γ_{sites} obtained for highly active $LaMnO_3$ nanoparticles,[21] which is at least three times larger than the pyrochlores reported herein due to the higher specific surface area of $LaMnO_3$.

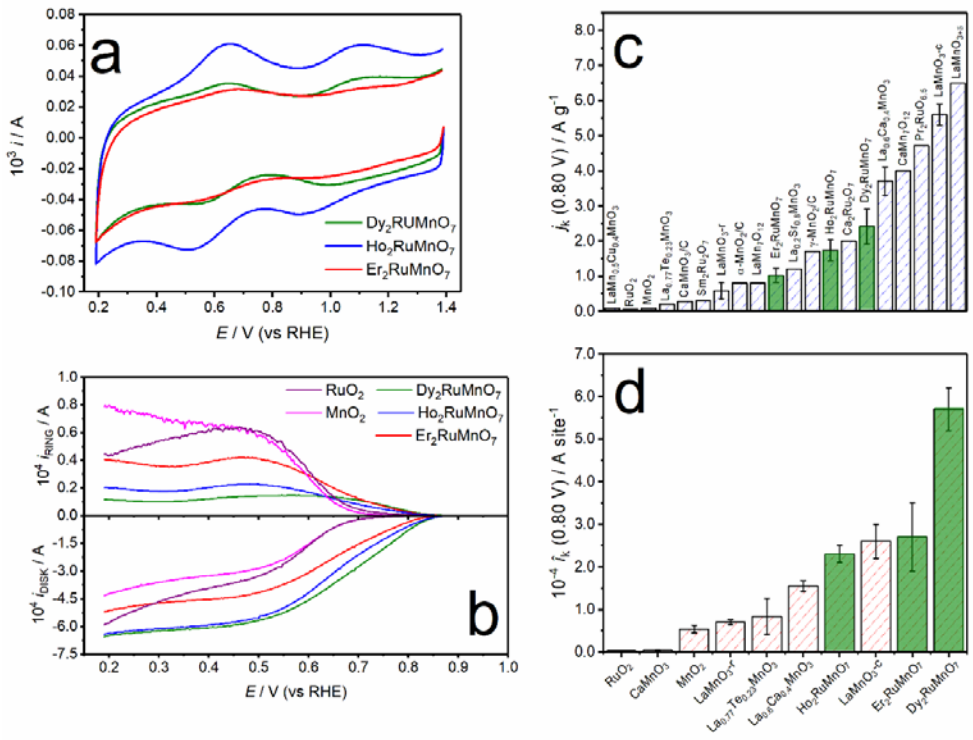

Figure 4. Pseudocapacitive responses and electrochemical activity of pyrochlores: (a) Cyclic voltammograms of Ho_2RuMnO_7, Dy_2RuMnO_7, and Er_2RuMnO_7 nanoparticles supported on mesoporous carbon electrodes (250 μg cm^{-2}) in Ar-saturated 0.1 M KOH solution at 0.10 V s^{-1}. The voltametric features correspond to the population and depopulation of Ru and Mn *d*-orbitals across the potential range. (b) Rotating ring-disc electrode (RRDE) studies of the carbon-supported pyrochlores at 1600 rpm in O_2-saturated 0.1 M KOH at 0.010 V s^{-1}. The Pt ring was held at a constant potential of 1.10 V. The oxide loading in each electrode was 250 μg cm^{-2}. (c) Kinetically limiting current at 0.80 V vs RHE normalized by the oxide mass at the electrode and benchmarking with some of the most active oxide reported $LaMn_{0.5}Cu_{0.5}O_3$,[33] $La_{0.77}Te_{0.23}MnO_3$,[19] $CaMnO_3$/C,[34] $Sm_2Ru_2O_7$ and $Pb_2RuO_{6.5}$,[35] $LaMnO_3$-r,[17] α-MnO_2/C and γ-MnO_2/C,[36] $LaMn_7O_{12}$ and $CaMn_7O_{12}$,[37] $La_{0.2}Sr_{0.8}MnO_3$,[38] $Ca_2Ru_2O_7$,[39] $La_{0.6}Ca_{0.4}MnO_3$,[21] $LaMnO_3$-c,[21] $LaMnO_{3+\delta}$.[9] (d) Kinetically limited current at 0.80 V vs RHE the electrode normalized by the number of active sites estimated from the pseudocapacitive charge in the absence of oxygen.

Characteristic current responses recorded on a rotating ring (Pt) - disk (pyrochlore supported on mesoporous carbon) electrode at a rotation rate of 1600 rpm and 0.010 V s^{-1} in O_2-saturated 0.1 M KOH are shown in **figure 4b**. Data obtained for commercial MnO_2 and RuO_2 oxides under the same conditions are also shown for comparison. The ORR onset potential at the disk electrode is at 0.86 V, which is over 150 mV more positive than for the monometallic oxides. Larger ring currents are also seen in the case of RuO_2 and MnO_2, suggesting an important contribution of the 2-electron reduction to hydrogen peroxide. Indeed, the hydrogen peroxide yield (**Figure S10**) observed in the case of Dy_2RuMnO_7 and Ho_2RuMnO_7 is below 20% at potentials more negative than 0.6 V. **Figure S11** contrasts the RRDE profiles of the Vulcan support with those obtained in the presence of the pyrochlores. Interestingly, the onset potential of hydrogen peroxide formation is about 100 mV more positive in the presence of the pyrochlore nanostructures. Er_2RuMnO_7 displays a higher hydrogen peroxide yield, which further suggests a lower activity towards the 4-electron ORR.

Figure 4c contrasts the kinetically limited (i_k) current, estimated from Koutecky-Levich plots (**see figure S12**), obtained for the three pyrochlores with the performance reported for some on the most active oxides in the literature. Considering the kinetically limited current at 0.80 V vs RHE normalized by mass, we can see the trend Dy_2RuMnO_7 > Ho_2RuMnO_7 > Er_2RuMnO_7, which agrees well with our previous observation on the A:B site ratio as a function of the lanthanide cation. It is also seen that the three pyrochlores benchmark positively with respect to some of the most active ORR metal oxide electrocatalysts, including $LaMnO_3$,[21] $LaMn_{0.5}Ni_{0.5}O_3$,[9] and α-MnO_2/C[40] electrodes.[25] However, this comparison ignores key experimental parameters such as specific surface area and surface composition. **Figure 4d** illustrates a more accurate comparison based on the number of active sites calculated from pseudocapacitive responses (see **table S6**). It

should be noted that all the data shown in **figure 4d** were analyzed and collected using the same methodology as described in this work, which provides a more self-consistent analysis. Based on this approach, which is equivalent to calculating the turn over frequency,[41] it can be seen that Er_2RuMnO_7 and Ho_2RuMnO_7 show similar activity as some of the most active $LaMnO_3$ oxide,[21] while Dy_2RuMnO_7 particles effectively double the ORR activity per site.

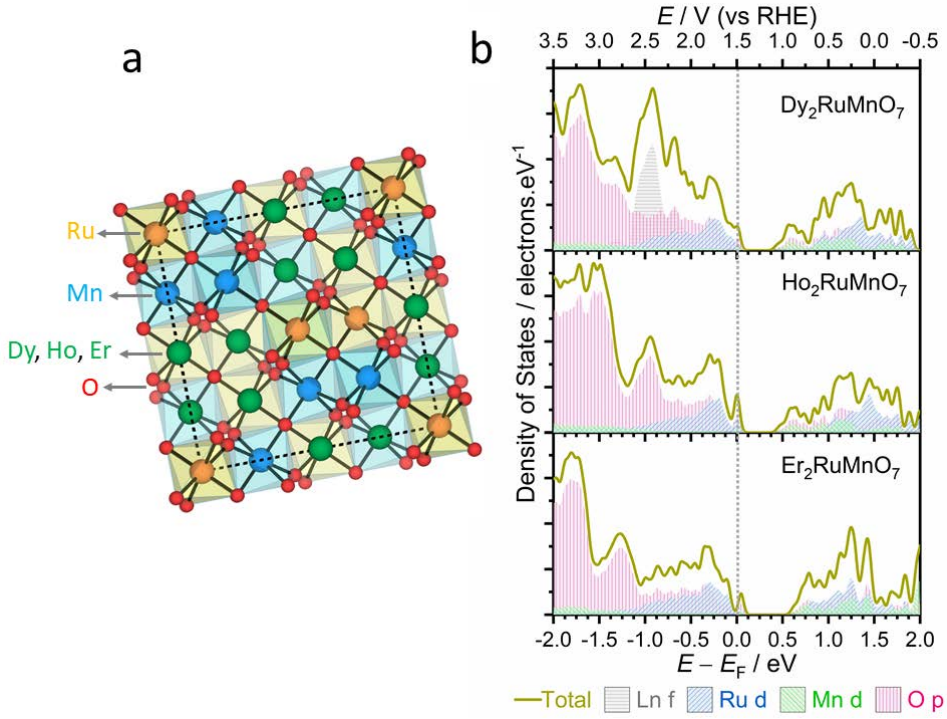

Figure 5. Electronic structure calculations: (a) 120 atoms supercell optimized employing DFT+U formalism using PBE (GGA) functionals, considering 5% occupancy of Mn in the *A*-site; (b) partial density of states calculations near the Fermi energy for the three pyrochlores. The potential scale is estimated from the onset potential for populating Ru and Mn *d*-orbitals obtained from voltametric profiles (see figure 4). In all cases, Ru and Mn d-orbitals overlap at the conduction band edge which is close to the standard ORR redox energy.

DISCUSSION

Activity as a function of the electronic structure – orbital mixing. We rationalize the high site activity of these pyrochlores in terms of the building up of density states at energies relevant to the ORR, which can be demonstrated by electronic structure calculations obtained by the DFT+U formalism using PBE (GGA) functionals as shown in **figure 5**. The structure of supercells containing 120 atoms was optimized (**figure 5a**) considering 5% Mn occupancy at the *A*-site, achieving a difference below 1.2% with respect to the experimental lattice parameters.[42] **Figure 5b** reveals a small bandgap below 0.5 eV for all three pyrochlores, which is consistent with the electrical measurements reported by Martinez-Coronado et al.,[42] taking into account temperature corrections. Focusing our attention into the conduction band region, which is relevant to the ORR, we can see the overall line shape exhibits two maxima containing contributions from Mn and Ru *d*-orbitals as well as O *p*-orbitals, suggesting a high degree of covalency. Partial DOS calculated over a wide range of energies are displayed in **figure S13**. The lanthanide orbitals are highly localized and far away from the energy range relevant for oxygen electrocatalysis.

The two broad features arising from the convolution of orbitals in the conduction band (approximately between 0.4 and 1.5 eV vs E_f) can be related to the voltammetric responses observed for the various pyrochlores in Ar-saturated solutions (**figure 4a**), i.e. the reduction current peaks observed as the potential is swept negatively correspond to filling up the DOS at the conduction band. This allows constructing an electrochemical potential scale, wherein the conduction band minimum (CBM) located around 1.2-1.3 V vs RHE strongly overlaps with the standard potential for the ORR to OH^-. This is the key observation underpinning the high site activity of the A_2RuMnO_7 pyrochlores. Not only do the *d*-orbitals of the B-sites overlap creating a large DOS but also the DOS is located at the thermodynamic energy required for the ORR,

fulfilling the boundary conditions established by the Gerischer model.[23-24, 43] This is clearly seen in the case of Dy_2RuMnO_7, which exhibits a 1:1 surface ratio of Mn and Ru from the XPS analysis. On the other hand, Ho_2RuMnO_7 and Er_2RuMnO_7 show Mn and Er surface excess, respectively, which slightly dampens the B-site activity enhancement.

On the basis of this analysis, we also anticipate a higher activity towards the oxygen evolution reaction (OER) in the case of Dy_2RuMnO_7, which exhibits a higher Ru surface ratio. Indeed, the DOS at the valence band maximum (VBM) is further enhanced by the presence of Ru *d*-orbitals, as shown in **figure 5b**. Current-voltage curves recorded under identical conditions reveal that the overpotential for achieving 10 mA cm^{-2}_{oxide} follows the trend Dy_2RuMnO_7 < Ho_2RuMnO_7 < Er_2RuMnO_7 (see **figure S15**), which exactly follows the trend in terms of Ru surface composition. Furthermore, the onset potential for OER is at 1.5 V vs RHE, which also coincides with the VBM position from our DFT calculations. It should be considered that in addition to the intrinsic errors associated with band gap estimations by DFT, these values effectively correspond to 0 K conditions. Furthermore, there is a component associated with the charging energy of the system upon populating/depopulating the CBM and VBM, respectively, which is implicitly considered in our approximation. However, despite the limitations of our analysis, correlation between bulk electronic structure from supercell DFT calculations and electrochemical responses enables identifying the nature of the key orbitals involved in the ORR and the OER. In order to formulate a more comprehensive mechanistic model, slab DFT calculations should be implemented (validated by surface structure analysis) incorporating water as a continuum[44] or explicitly,[45] which is a formidable challenge for such complex oxide structures.

CONCLUSIONS

Pyrochlores with the general formula A_2RuMnO_7, where A = Dy^{3+}, Ho^{3+} and Er^{3+} show enhanced electrocatalytic activity in alkaline electrolyte due to a strong overlap of Ru and Mn *d*-orbitals as well as O *p*-orbitals in the energy range relevant to oxygen electrochemistry. Our detailed analysis based on XAS and XES concluded that the various lanthanides introduce rather subtle variations in M-O bonding distances (below 1%), and slight changes in the effective bulk oxidation state of Mn-sites. On the other hand, XPS and electrochemical analysis do show a stronger dependence of the surface composition with the *A*-site cation, which has a direct impact on the effective electrocatalytic activity. From the three pyrochlores, Dy_2RuMnO_7 exhibits a Ru/Mn surface ratio closer to 1, which we consider as optimal for activity site enhancement towards oxygen electrocatalysis via orbital mixing. Electrochemical studies supported by electronic structure calculations based on DFT calculations conclude that not only do the CBM and VBM exhibit strong overlap of Ru, Mn and O orbitals (high-degree of covalency), but also their DOS are located close the formal oxygen redox energy, which leads to the highest electrocatalytic activity per surface redox site reported.

METHODS

Pyrochlores preparation. A_2MnRuO_7 (A = Dy, Ho, Er) oxides were prepared by a wet chemistry procedure inspired by the work of Martinez-Coronado et al.[26] Briefly, stoichiometric amounts of A_2O_3, $MnCO_3$ and RuO_2 were dissolved in citric acid (10%) and some drops of nitric acid. The solution was then slowly evaporated, leading an organic resin. The formed resins were dried at 120 °C and decomposed at 600 °C for 12 h and 800 °C for 2 h in order to eliminate the organic materials and the nitrates. This treatment gave rise to finely divided and homogeneous precursor materials that finally were heated in air at 900 °C for 12 h to obtain the pure pyrochlore oxide phase.

X-ray Diffraction. X-ray diffraction (XRD) patterns were recorded using a Bruker AXS D8 Advance diffractometer with a θ-θ configuration, using Cu Kα radiation (λ = 0.154 nm). Experiments were run between 20 and 90 degrees, using a step size of 0.02 degrees.

Transmission Electron Microscopy. Transmission electron microscopy (TEM) and high resolution TEM analysis were obtained using a JEOL JEM-1400Plus and a JEOL JEM 2010, respectively. Samples for TEM were produced by placing 1 mL drops of the oxide particles dissolved in ethanol on a 3 mm diameter carbon-coated copper grid. Mean particle diameters were estimated from at least 100 nanoparticles per sample.

X-Ray photoemission spectroscopy. Photoemission data was obtained in a custom designed UHV system equipped with an EA 125 Omicron electron analyzer with five channeltrons, working at a base pressure of 10^{-10} mbar. Core level photoemission spectra (Er 4*d*, Dy 4*d*, Ho 4*d*, Ru 3*d*/C 1*s*, Ru 3*p*, O 1*s* and Mn 2*p*) were collected in normal emission at room temperature with a non-monochromatized Mg K_α X-ray source (1253.6 eV) and using 0.1 eV steps, 0.5 s collection time and 20 eV pass energy. Gaussian/Lorentzian lines are used to deconvolute XPS spectra with Shirley background correction. The sensitivity factors were calculated from the corresponding cross section, asymmetry and inelastic mean free path for each of the region associated with these specific materials.

Extended X-ray absorption fine structure (EXAFS) and X-ray emission spectroscopy (XES). EXAFS spectra were recorded in transmission mode at the Mn K edge (6539 eV) and Ru K edge (22117 eV), on beamline B18 at the Diamond Light Source operating with a ring energy 3 GeV and at a current of 300 mA. The monochromator comprises a Si(111)/Si(311) crystals operating in Quick EXAFS mode. Calibration of the monochromator was carried out using a Mn and Ru foils. The samples were prepared as pellets (1.32 cm^2 area pellet) by mixing the ground

sample with cellulose (~80 mg) to form a homogenous mixture, and then compressed (~5 Ton) using a pellet press. A total of three spectra were averaged for each sample. The data was analysed using the Athena and Arthemis programs.[46] The spectra were aligned using the Mn foil response.

X-ray emission spectroscopy (XES) measurements were conducted at Beamline I20-scanning, of Diamond Light Source.[47-48] The beamline is equipped with an in-house designed four-bounce scanning Si(111) monochromator, and the harmonic rejection was achieved by using two Rh-coated mirrors. An X-ray emission spectrometer based on a 1 m diameter Rowland circle operating in the Johann configuration in the vertical plane with 3 Ge(440) crystals used to collect the emission signal was used for the experiment. The XES spectra have been normalized with respect to their total area using the range 6465-6497 eV.

Electrocatalytic studies. Electrochemical measurements were conducted in a three electrode cell using a rotating ring-disk electrode (RRDE) fitted to an ALS rotation controller and connected to a CompactStat bipotentiostat (Ivium). The RRDE electrode consisted of a 4 mm glassy carbon disk surrounded by a Pt ring. The collection efficiency was experimentally determined to be 0.4. Hg/HgO (in 1 M NaOH, IJ Cambria) was used as the reference electrode. The potentials in this work have been converted in reference to a RHE. Measurements were carried out in 0.1 M KOH saturated with either purified Ar or O_2 (BOC). A thin-film catalyst layer was deposited on the glassy carbon electrode using a two-step drop-casting method with two different inks, as previously described.[21] The final loading in the catalyst layer for each electrode was controlled at 250 μg_{OXIDE} cm^{-2}, 50 μg_{VULCAN} cm^{-2} and 50 μg_{NAFION} cm^{-2} (per geometric surface area of the electrode).

The peroxide yield, $X_{HO_2^-}$, can be calculated as from:

$$X_{HO_2^-} = \frac{2\frac{i_{RING}}{N}}{i_{DISK}+\frac{i_{RING}}{N}} \times 100 \quad (1)$$

where i_{DISK} is the current at the disk, i_{RING} is the current at the ring, and N is the collection coefficient.

The Kouteckly-Levich relationship describes the dependence of the disk current (i_{DISK}) on the angular rotation rate (ω):

$$\frac{1}{i_{DISK}} = \frac{1}{i_k} + \frac{1}{i_L} = \frac{1}{i_k} + \frac{1}{0.62nAFcD^{2/3}\nu^{-1/6}\omega^{1/2}} \quad (2)$$

where i_k and i_L are the kinetically and mass-transport limiting current, n is the number of transferred electrons, D is the oxygen diffusion coefficient (D = 1.9· 10^{-5} cm^2 s^{-1}), c is the bulk oxygen concentration (c =1.2·10^{-6} mol cm^{-3}), and ν is the kinematic viscosity (ν = 0.01 cm^2 s^{-1}). Other parameters in equation (2) are the disk geometric area (A) and the Faraday constant (F).

Computational methods. Structure optimisation of three pyrochlores was performed under DFT+U formalism as defined in CASTEP code.[49-50] A 120-atom supercell is used with 1:1 Mn, and Ru substituted B-site while the lanthanide *A*-site is substituted with 5% Mn, to mimic the experimental structure reported.[42] A GGA-PBE functional with a Monkhorst-Pack k-point grid of spacing <0.025 $Å^{-1}$ and Norm-conserving pseudopotentials is implemented with energy cut-off of 1000 eV. Tight convergence criteria are enforced including 1 meV/Å for forces and 1 × 10^{-8} eV for energy. The Hubbard parameters $U_{\text{effective}}$ ($U - J$) used for Ru and Mn d-orbitals are 2.4 eV and 3.0 eV based on previous works.[51-52] While the $U_{\text{effective}}$ for all three lanthanides is taken as 6.5 eV based on the work of Huang.[53] The optimised structure belong to cubic-lattice (space-group: Fd-3m), showing the following lattice parameters (experimental values in parenthesis from reference[25]): Dy_2RuMnO_7 = 10.1194 Å (10.0816 Å); Er_2RuMnO_7 = 9.9165 Å (10.0224 Å);

Ho_2RuMnO_7 = 10.1688 Å (10.0491 Å). Thus, optimised structures have an excellent agreement with the structural parameters derived from the neutron diffraction of synthesised powders. The density of states (DOS) are calculated using the same input calculation parameters as used for structural optimisation. Similar to geometry results, the estimated bandgaps are in close agreement with activation energies for the electrical conductivity.

ASSOCIATED CONTENT

Supporting Information.

The Supporting Information is available free of charge at https://pubs.acs.org/doi/10.1021/

Figure S1. Particle size distribution of pyrochlores nanostructures. **Figure S2.** High-resolution TEM images of Er_2RuMnO_7 nanoparticles. **Figure S3.** High-resolution TEM images of Ho_2RuMnO_7 and Dy_2RuMnO_7. **Figure S4.** Mn pre-edge XANES features of pyrochlores and references. **Figure S5.** Mn Kβ XES spectra of pyrochlores and references. **Figure S6.** linear combination fit of the Mn Kβ XES spectra of pyrochlores. **Figure S7.** k^2 weighted χ data and k^2 weighted Fourier transform EXAFS data of the Mn and Ru K edge. **Figure S8.** Dy 4*d*, Ho 4*d*, Er 4*d*, Ru 3*d*/C1*s* and O 1s X-ray photoemission spectra. **Figure S9.** Estimation of the Faradaic charges by integration of electrochemical responses. **Figure S10.** HO_2^- yields during ORR for all pyrochlores catalysts and binary oxides. **Figure S11.** Comparison of pyrochlores' ORR electrochemical signals with a Vulcan electrode. **Figure S12.** Koutecky-Levich plots for ORR at Vulcan supported pyrochlores. **Figure S13.** Partial DOS calculated for the various pyrochlores employing DFT-U. **Figure S14.** Linear Sweep Voltammetry for the oxygen evolution reaction at carbon supported pyrochlores. **Table S1.** Density, mean particle diameters and specific surface

area of the pyrochlore nanoparticles. **Table S2.** Structural parameters obtained from the refining Mn K and the Ru K EXAFS data. **Table S3**. Analysis of the Ru 3*p* photoemission line for the A_2RuMnO_7 samples. **Table S4**. Surface A:Ru:Mn atomic ratios as obtained by XPS. **Table S5**. Faradic charge associated with the reduction of surface sites and number density of active sites (Γ_{sites}). **Table S6.** Kinetically limiting current at 0.80 V vs RHE normalised by the effective number of active sites at the surface, mass of oxide at the electrode and the area of oxide present at the electrode.

AUTHOR INFORMATION

Corresponding Authors

*Veronica Celorrio. E-mail: veronica.celorrio@diamond.ac.uk

*Devendra Tiwari: devendra.tiwari@northumbria.ac.uk

*David J. Fermín. E-mail: David.Fermin@bristol.ac.uk

Notes.

The authors declare no competing financial interest. All data created during this study are openly available from the University of Bristol Research Data Repository at https://doi.org/

ACKNOWLEDGEMENTS

VC, AER, AA and DJF kindly thank the UK Catalysis Hub for resources and support provided via the membership of the UK Catalysis Hub Consortium and funded by EPSRC (EPSRC grants EP/K014706/1 and EP/K014714/1). TEM studies were carried out at the University of Bristol Chemistry Imaging Facility with equipment funded by UoB and EPSRC (EP/K035746/1 and EP/M028216/1). The authors wish to acknowledge the Diamond Light Source for provision of beamtime (SP10306, SP15151 and SP16479). VC is in debt to the STFC Batteries Network (ST/N002385/1) for support through an STFC Batteries Early Career Award. DT and DJF are

grateful to the University of Bristol's high-performance computing facility at the Advanced Computing Research Centre for enabling the computational work. DT also acknowledges the support from EPSRC for funding through grant EP/R021503/1 (The North East Centre for Energy Materials).

REFERENCES

1. Herranz, J.; Durst, J.; Fabbri, E.; Patru, A.; Cheng, X.; Permyakova, A. A.; Schmidt, T. J., Interfacial effects on the catalysis of the hydrogen evolution, oxygen evolution and CO2-reduction reactions for (co-)electrolyzer development. *Nano Energy* **2016,** *29*, 4-28.

2. De Luna, P.; Hahn, C.; Higgins, D.; Jaffer, S. A.; Jaramillo, T. F.; Sargent, E. H., What would it take for renewably powered electrosynthesis to displace petrochemical processes? *Science* **2019,** *364*, 350.

3. Higgins, D.; Hahn, C.; Xiang, C.; Jaramillo, T. F.; Weber, A. Z., Gas-Diffusion Electrodes for Carbon Dioxide Reduction: A New Paradigm. *ACS Energy Lett.* **2019,** *4*, 317-324.

4. Mathew, V.; Sambandam, B.; Kim, S.; Kim, S.; Park, S.; Lee, S.; Alfaruqi, M. H.; Soundharrajan, V.; Islam, S.; Putro, D. Y.; Hwang, J.-Y.; Sun, Y.-K.; Kim, J., Manganese and Vanadium Oxide Cathodes for Aqueous Rechargeable Zinc-Ion Batteries: A Focused View on Performance, Mechanism, and Developments. *ACS Energy Lett.* **2020,** *5*, 2376-2400.

5. Sun, C.; Alonso, J. A.; Bian, J., Recent Advances in Perovskite-Type Oxides for Energy Conversion and Storage Applications. *Adv. Energy Mater.* **2020,** *10.1002/aenm.202000459*.

6. Calvillo, L.; Carraro, F.; Vozniuk, O.; Celorrio, V.; Nodari, L.; Russell, A. E.; Debellis, D.; Fermin, D.; Cavani, F.; Agnoli, S.; Granozzi, G., Insights into the durability of Co–Fe spinel oxygen evolution electrocatalysts via operando studies of the catalyst structure. *J. Mater. Chem. A* **2018,** *6*, 7034-7041.

7. Sardar, K.; Petrucco, E.; Hiley, C. I.; Sharman, J. D. B.; Wells, P. P.; Russell, A. E.; Kashtiban, R. J.; Sloan, J.; Walton, R. I., Water-Splitting Electrocatalysis in Acid Conditions Using Ruthenate-Iridate Pyrochlores. *Angew. Chem. Int. Ed.* **2014,** *53*, 10960-10964.

8. Liu, J.; Liu, H.; Chen, H.; Du, X.; Zhang, B.; Hong, Z.; Sun, S.; Wang, W., Progress and Challenges Toward the Rational Design of Oxygen Electrocatalysts Based on a Descriptor Approach. *Adv. Sci.* **2020,** *7*, 1901614.

9. Suntivich, J.; Gasteiger, H. A.; Yabuuchi, N.; Nakanishi, H.; Goodenough, J. B.; Shao-Horn, Y., Design principles for oxygen-reduction activity on perovskite oxide catalysts for fuel cells and metal–air batteries. *Nat Chem* **2011,** *3*, 546-550.

10. Ji, Q.; Bi, L.; Zhang, J.; Cao, H.; Zhao, X. S., The role of oxygen vacancies of ABO3 perovskite oxides in the oxygen reduction reaction. *Energy Environ. Sci.* **2020,** *13*, 1408-1428.

11. Hong, W. T.; Stoerzinger, K. A.; Lee, Y.-L.; Giordano, L.; Grimaud, A.; Johnson, A. M.; Hwang, J.; Crumlin, E. J.; Yang, W.; Shao-Horn, Y., Charge-transfer-energy-dependent oxygen evolution reaction mechanisms for perovskite oxides. *Energy Environ. Sci.* **2017,** *10*, 2190-2200.

12. Stoerzinger, K. A.; Hong, W. T.; Wang, X. R.; Rao, R. R.; Bengaluru Subramanyam, S.; Li, C.; Ariando; Venkatesan, T.; Liu, Q.; Crumlin, E. J.; Varanasi, K. K.; Shao-Horn, Y., Decreasing the Hydroxylation Affinity of La1–xSrxMnO3 Perovskites To Promote Oxygen Reduction Electrocatalysis. *Chemistry of Materials* **2017,** *29*, 9990-9997.

13. Hong, W. T.; Risch, M.; Stoerzinger, K. A.; Grimaud, A.; Suntivich, J.; Shao-Horn, Y., Toward the rational design of non-precious transition metal oxides for oxygen electrocatalysis. *Energy Environ. Sci.* **2015,** *8*, 1404-1427.

14. Bradley, K.; Giagloglou, K.; Hayden, B. E.; Jungius, H.; Vian, C., Reversible perovskite electrocatalysts for oxygen reduction/oxygen evolution. *Chem. Sci.* **2019,** *10*, 4609-4617.

15. V, V. M.; Nageswaran, G., Operando X-Ray Spectroscopic Techniques: A Focus on Hydrogen and Oxygen Evolution Reactions. *Front. Chem.* **2020,** *8*, 10.3389/fchem.2020.00023.

16. Crumlin, E. J.; Liu, Z.; Bluhm, H.; Yang, W.; Guo, J.; Hussain, Z., X-ray spectroscopy of energy materials under in situ/operando conditions. *J. Electron. Spectrosc. Relat. Phenom.* **2015,** *200*, 264-273.

17. Celorrio, V.; Calvillo, L.; van den Bosch, C. A. M.; Granozzi, G.; Aguadero, A.; Russell, A. E.; Fermín, D. J., Mean Intrinsic Activity of Single Mn Sites at LaMnO3 Nanoparticles Towards the Oxygen Reduction Reaction. *ChemElectroChem* **2018,** *5*, 3044-3051.

18. Celorrio, V.; Dann, E.; Calvillo, L.; Morgan, D. J.; Hall, S. R.; Fermin, D. J., Oxygen Reduction at Carbon-Supported Lanthanides: The Role of the B-Site. *ChemElectroChem* **2016,** *3*, 283-291.

19. Celorrio, V.; Morris, L. J.; Cattelan, M.; Fox, N. A.; Fermin, D. J., Tellurium-doped lanthanum manganite as catalysts for the oxygen reduction reaction. *MRS Commun.* **2017,** *7*, 193-198.

20. Gobaille-Shaw, G. P. A.; Celorrio, V.; Calvillo, L.; Morris, L. J.; Granozzi, G.; Fermin, D. J., Effect of Ba content on the activity of $La_{1-x}Ba_xMnO_3$ towards the oxygen reduction reaction. *ChemElectroChem* **2018,** *5*, 1922-1927.

21. Celorrio, V.; Calvillo, L.; Dann, E.; Granozzi, G.; Aguadero, A.; Kramer, D.; Russell, A. E.; Fermin, D. J., Oxygen reduction reaction at $La_xCa_{1-x}MnO_3$ nanostructures: interplay between A-site segregation and B-site valency. *Catal. Sci. Technol.* **2016,** *6*, 7231-7238.

22. Celorrio, V.; Calvillo, L.; Granozzi, G.; Russell, A. E.; Fermin, D. J., AMnO3 (A = Sr, La, Ca, Y) Perovskite Oxides as Oxygen Reduction Electrocatalysts. *Top. Catal.* **2018,** *61*, 154-161.

23. Gerischer, H., Über den Ablauf von Redoxreaktionen an Metallen und an Halbleitern. *Z. Phys. Chem.* **1960,** *26*, 223.

24. Gerischer, H., Über den Ablauf von Redoxreaktionen an Metallen und an Halbleitern. *Z. Phys. Chem.* **1961,** *27*, 48.

25. Stoerzinger, K. A.; Risch, M.; Han, B.; Shao-Horn, Y., Recent Insights into Manganese Oxides in Catalyzing Oxygen Reduction Kinetics. *ACS Catal.* **2015,** *5*, 6021-6031.

26. Martínez-Coronado, R.; Aguadero, A.; de la Calle, C.; Fernández, M. T.; Alonso, J. A., Evaluation of the R_2RuMnO_7 pyrochlores as cathodes in solid-oxide fuel cells. *J. Power Sources* **2011,** *196*, 4181-4186.

27. Bordage, A.; Trannoy, V.; Proux, O.; Vitoux, H.; Moulin, R.; Bleuzen, A., In situ site-selective transition metal K-edge XAS: a powerful probe of the transformation of mixed-valence compounds. *Phys. Chem. Chem. Phys.* **2015,** *17*, 17260-17265.

28. Berti, G.; Sanna, S.; Castellano, C.; Van Duijn, J.; Ruiz-Bustos, R.; Bordonali, L.; Bussetti, G.; Calloni, A.; Demartin, F.; Duò, L.; Brambilla, A., Observation of Mixed Valence Ru Components in Zn Doped $Y_2Ru_2O_7$ Pyrochlores. *J. Phys. Chem. C* **2016,** *120*, 11763-11768.

29. Mefford, J. T.; Hardin, W. G.; Dai, S.; Johnston, K. P.; Stevenson, K. J., Anion charge storage through oxygen intercalation in LaMnO3 perovskite pseudocapacitor electrodes. *Nature Materials* **2014,** *13*, 726-732.

30. Grumelli, D.; Wiegmann, T.; Barja, S.; Reikowski, F.; Maroun, F.; Allongue, P.; Balajka, J.; Parkinson, G. S.; Diebold, U.; Kern, K.; Magnussen, O. M., Electrochemical Stability of the Reconstructed Fe3O4(001) Surface. *Angew. Chem. Int. Ed.* **2020,** *59*, 21904-21908.

31. Browne, M. P.; Colavita, P. E.; Lyons, M. E. G., Low Overpotential, High Activity: Manganese/ Ruthenium Mixed Oxide Electrocatalysts for Oxygen Evolution in Alkaline Media. *ECS Trans.* **2015,** *64*, 143-154.

32. Lyons, M. E. G.; Floquet, S., Mechanism of oxygen reactions at porous oxide electrodes. Part 2-Oxygen evolution at RuO_2, IrO_2 and $Ir_xRu_{1-x}O_2$ electrodes in aqueous acid and alkaline solution. *Phys. Chem. Chem. Phys.* **2011,** *13*, 5314-5335.

33. Suntivich, J.; Gasteiger, H. A.; Yabuuchi, N.; Shao-Horn, Y., Electrocatalytic Measurement Methodology of Oxide Catalysts Using a Thin-Film Rotating Disk Electrode. *J. Electrochem. Soc.* **2010,** *157*, B1263.

34. Hancock, C. A.; Ong, A. L.; Slater, P. R.; Varcoe, J. R., Development of CaMn1-xRuxO3-y (x = 0 and 0.15) oxygen reduction catalysts for use in low temperature electrochemical devices containing alkaline electrolytes: ex situ testing using the rotating ring-disk electrode voltammetry method. *J. Mater. Chem. A* **2014,** *2*, 3047-3056.

35. Park, J.; Risch, M.; Nam, G.; Park, M.; Shin, T. J.; Park, S.; Kim, M. G.; Shao-Horn, Y.; Cho, J., Single crystalline pyrochlore nanoparticles with metallic conduction as efficient bi-functional oxygen electrocatalysts for Zn-air batteries. *Energy Environ. Sci.* **2017,** *10*, 129-136.

36. Meng, Y.; Song, W.; Huang, H.; Ren, Z.; Chen, S.-Y.; Suib, S. L., Structure–Property Relationship of Bifunctional MnO2 Nanostructures: Highly Efficient, Ultra-Stable Electrochemical Water Oxidation and Oxygen Reduction Reaction Catalysts Identified in Alkaline Media. *J. Am. Chem. Soc.* **2014,** *136*, 11452-11464.

37. Yamada, I.; Fujii, H.; Takamatsu, A.; Ikeno, H.; Wada, K.; Tsukasaki, H.; Kawaguchi, S.; Mori, S.; Yagi, S., Bifunctional Oxygen Reaction Catalysis of Quadruple Manganese Perovskites. *Adv. Mater.* **2017,** *29*, 1603004.

38. Tulloch, J.; Donne, S. W., Activity of perovskite La1−xSrxMnO3 catalysts towards oxygen reduction in alkaline electrolytes. *J. Power Sources* **2009,** *188*, 359-366.

39. Hancock, C. A.; Ong, A. L.; Varcoe, J. R., Effect of carbonate anions on Bi-doped Ca2Ru2O7 pyrochlores that are potential cathode catalysts for low temperature carbonate fuel cells. *RSC Advances* **2014,** *4*, 30035-30045.

40. Cheng, F.; Su, Y.; Liang, J.; Tao, Z.; Chen, J., MnO2-Based Nanostructures as Catalysts for Electrochemical Oxygen Reduction in Alkaline Media. *Chemistry of Materials* **2010,** *22*, 898-905.

41. Stevens, M. B.; Enman, L. J.; Batchellor, A. S.; Cosby, M. R.; Vise, A. E.; Trang, C. D. M.; Boettcher, S. W., Measurement Techniques for the Study of Thin Film Heterogeneous Water Oxidation Electrocatalysts. *Chemistry of Materials* **2017,** *29*, 120-140.

42. Martinez-Coronado, R.; Retuerto, M.; Fernandez, M. T.; Alonso, J. A., Evolution of the crystal and magnetic structure of the R2MnRuO7 (R = Tb, Dy, Ho, Er, Tm, Yb, Lu, and Y) family of pyrochlore oxides. *Dalton Trans.* **2012,** *41*, 8575-8584.

43. Kissling, G. P.; Miles, D. O.; Fermín, D. J., Electrochemical charge transfer mediated by metal nanoparticles and quantum dots. *Phys. Chem. Chem. Phys.* **2011,** *13*, 21175-21185.

44. Tiwari, D.; Alibhai, D.; Cherns, D.; Fermin, D. J., Crystal and Electronic Structure of Bismuth Thiophosphate, BiPS4: An Earth-Abundant Solar Absorber. *Chemistry of Materials* **2020,** *32*, 1235-1242.

45. Bhati, M.; Chen, Y.; Senftle, T. P., Density Functional Theory Modeling of Photo-electrochemical Reactions on Semiconductors: H2 Evolution on 3C-SiC. *J. Phys. Chem. C* **2020,** *124*, 26625-26639.

46. Ravel, B.; Newville, M., ATHENA, ARTEMIS, HEPHAESTUS: data analysis for X-ray absorption spectroscopy using IFEFFIT. *J. Synchrotron Rad.* **2005,** *12*, 537-541.

47. Diaz-Moreno, S.; Amboage, M.; Basham, M.; Boada, R.; Bricknell, N. E.; Cibin, G.; Cobb, T. M.; Filik, J.; Freeman, A.; Geraki, K.; Gianolio, D.; Hayama, S.; Ignatyev, K.; Keenan, L.; Mikulska, I.; Mosselmans, J. F. W.; Mudd, J. J.; Parry, S. A., The Spectroscopy Village at Diamond Light Source. *J. Synchrotron Rad.* **2018,** *25*, 998-1009.

48. Hayama, S.; Duller, G.; Sutter, J. P.; Amboage, M.; Boada, R.; Freeman, A.; Keenan, L.; Nutter, B.; Cahill, L.; Leicester, P.; Kemp, B.; Rubies, N.; Diaz-Moreno, S., The scanning four-bounce monochromator for beamline I20 at the Diamond Light Source. *J. Synchrotron Rad.* **2018,** *25*, 1556-1564.

49. Payne, M. C.; Teter, M. P.; Allan, D. C.; Arias, T. A.; Joannopoulos, J. D., Iterative minimization techniques for ab initio total-energy calculations: molecular dynamics and conjugate gradients. *Reviews of Modern Physics* **1992,** *64*, 1045-1097.

50. Clark, S. J.; Segall, M. D.; Pickard, C. J.; Hasnip, P. J.; Probert, M. I. J.; Refson, K.; Payne, M. C., First principles methods using CASTEP. *Zeitschrift für Kristallographie - Crystalline Materials* **2005,** *220*, 567.

51. Colizzi, G.; Filippetti, A.; Fiorentini, V., Magnetism of $La_{0.625}Sr_{0.375}MnO_3$ under high pressure from first principles. *Physical Review B* **2007,** *76*, 064428.

52. Dang, H. T.; Mravlje, J.; Georges, A.; Millis, A. J., Electronic correlations, magnetism, and Hund's rule coupling in the ruthenium perovskites $SrRuO_3$ and $CaRuO_3$. *Physical Review B* **2015,** *91*, 195149.

53. Huang, B., 4f fine-structure levels as the dominant error in the electronic structures of binary lanthanide oxides. *J. Comput. Chem.* **2016,** *37*, 825-835.